The Potential of Multifrequency Spaceborne DInSAR Measurements for the Retrieval of Snow Water Equivalent

Journal Article

Author(s):
Belinska, Kristina; Fischer, Georg ⓘD; Parrella, Giuseppe; Hajnsek, Irena ⓘD

The Potential of Multifrequency Spaceborne DInSAR Measurements for the Retrieval of Snow Water Equivalent

Kristina Belinska , *Graduate Student Member, IEEE*, Georg Fischer , Giuseppe Parrella ,
and Irena Hajnsek , *Fellow, IEEE*

Abstract—The snow water equivalent (SWE) is the amount of water contained in a snow pack and is, therefore, an important variable for hydrological and climate models. Differential interferometric synthetic aperture radar (DInSAR) techniques can relate the interferometric phase of two repeat-pass SAR acquisitions to the SWE change between them. However, only a limited interval of SWE change can be retrieved unambiguously due to phase wraps of the interferometric phase. This interval strongly depends on the wavelength of the radar wave. Additional information, for instance ground measurements of SWE, is required to identify whether the SWE change exceeded that interval and to correct the phase wraps. In the study, the performance of X-, C-, and L-bands spaceborne SAR acquisitions for SWE estimation is analyzed, demonstrating the advantages and limitations of different frequencies. Shorter wavelengths show a higher accuracy for SWE estimations, while longer wavelengths are less affected by phase wraps. A multifrequency approach is proposed where L-band acquisitions are used to correct the phase wraps in the C-band SWE retrieval. The accuracy decreases slightly, but this approach allows a more robust SWE retrieval without the need of additional ground measurements. For current spaceborne SAR missions, temporal decorrelation and phase calibration are limiting factors.

Index Terms—ALOS 2, dry snow, interferometric phase, Sentinel-1, snow water equivalent (SWE), synthetic aperture radar (SAR), TanDEM-X.

I. Introduction

THE seasonal snow cover is an essential variable for climate and hydrological models. While the high albedo and emissivity of snow have an important impact on the Earth's energy budget [1], increasing temperatures lead to accelerated melting

Kristina Belinska is with the Microwaves and Radar Institute, German Aerospace Center (DLR), 82234 Wessling, Germany, and also with the Institute of Environmental Engineering, Swiss Federal Institute of Technology in Zurich (ETH), 8093 Zürich, Switzerland (e-mail: kristina.belinska@dlr.de).

Georg Fischer is with the Microwaves and Radar Institute, German Aerospace Center (DLR), 82234 Wessling, Germany (e-mail: georg.fischer@dlr.de).

Giuseppe Parrella is with the European Space Agency (ESA), 00044 Frascati, Italy (e-mail: giuseppe.parrella@esa.int).

Irena Hajnsek is with the Institute of Environmental Engineering, Swiss Federal Institute of Technology in Zurich (ETH), 8093 Zürich, Switzerland, and also with the Microwaves and Radar Institute, German Aerospace Center (DLR), 82234 Wessling, Germany (e-mail: irena.hajnsek@dlr.de).

Digital Object Identifier 10.1109/JSTARS.2023.3345139

of snow, and also of land ice, which results in a sea level rise [2], [3].

Rising temperatures also cause the alteration of runoff regimes in mountainous areas, which has a high impact on regions where people rely on snowmelt for their water supply and water storage capabilities are not sufficient [4].

A parameter that can be used to characterize this is the snow water equivalent (SWE), which describes the amount of liquid water stored in a snow pack and is thus an important variable in hydrological models for runoff predictions [5].

Ground-based measurements of SWE provide precise information but can typically cover only small areas and are performed on a limited number of locations, as snow covered areas are often characterized by extreme weather conditions and are located in remote regions, which can be hard to access. A wider coverage is typically achieved by interpolation of sparsely sampled data, leading to large uncertainties and coarse spatial resolution.

However, the employment of remote sensing techniques enables a wide coverage and high temporal resolution. Microwave sensors offer the possibility to monitor the Earth's surface in a systematic way independently from sunlight illumination and weather conditions. This is particularly important for high latitude regions, which are affected by polar darkness [6] and often covered by clouds [7].

Passive microwave sensors like radiometers are able to deliver global snow products, including SWE, on a daily basis [8], [9]. The retrieval algorithms rely on the link between the brightness temperature and the presence of snow on the observed surface [10]. However, the snow signal measured by passive sensors saturates for deep snow packs [11]. In addition, the global daily coverage offered by such sensors is achieved at the cost of a spatial resolution on kilometer scale [12].

Active microwave sensors, on the other hand, like synthetic aperture radars (SARs), offer a spatial resolution on meter-scale [13], which is required for an accurate mapping of mountainous areas and heterogeneous landscapes and could significantly enhance SWE information products.

The sensitivity of SAR measurements to snow properties has been already demonstrated in early studies [14], [15] opening the way toward the retrieval of relevant parameters, such as snow depth and SWE.

Different SWE retrieval models based on radiative transfer models have been established [16], [17], [18]. In cases of wet snow, the retrieval of snow depth has also been attempted with single-pass radar interferometry by differencing two digital elevation models (DEMs) [19]. Other studies have shown that the polarizations of radar waves can be utilized for the retrieval of snow parameters [20], [21].

A promising and straightforward approach to retrieve SWE has been proposed first in [22], and then, in [23], exploiting differential interferometry (DInSAR) between two temporally separated SAR acquisitions. It relies on the fact that microwaves are refracted in dry snow, which has an effect on the interferometric phase. The theory shows that changes in SWE between two acquisitions cause a change in the path delay of the radar waves that provides a direct link between the temporal evolution of SWE and the interferometric phase measured by the SAR system. The model proposed in [22] has been further refined in [23] in order to extend its applicability to a wider range of snow densities.

The method has been successfully demonstrated using time-series data from a tower-based instrument measuring with a temporal baseline of 4 h [23] and also with a multifrequency tower-based experiment, analyzing the influence of environmental effects on the coherence [24].

The transferability of such an approach to the spaceborne case has been already assessed in several studies [25], [26], [27], [28]. Some of which showed that the revisit time of current missions is one of the main limiting factors, as well as the lack of validation data. However, only single-frequency measurements were assessed.

This study aims to provide further insights into the SWE estimation from multifrequency spaceborne data using the approach of [23]. Datasets at different frequencies, X-, C-, and L-bands, acquired by operational satellite SAR missions (TanDEM-X, Sentinel-1 and ALOS-2) are jointly exploited to assess the main aspects determining the performance, such as the temporal resolution and the different interferometric sensitivities. The estimated SWE values are compared to ground-based measurements from a test site in Finland. Particular emphasis is put on the estimation error due to phase wrapping of the interferometric phase. This is analyzed by utilizing the ground measurements for the phase wrap correction. Furthermore, a multifrequency solution is presented, where measurements with different frequencies are exploited to correct for missing phase cycles. Such a multifrequency approach reduces the necessity for external SWE information to solve phase wrapping, which is essential for future large scale spaceborne applications.

The rest of this article is organized as follows. In Section II, the model of [23] relating DInSAR measurements to SWE changes is described, and its frequency-dependent sensitivity is analyzed. Section III presents the employed experimental ground measurements and spaceborne SAR datasets as well as the processing steps. The results of the SWE estimation, including the ground-based and multifrequency phase wrap corrections, are reported and discussed in Section IV. Finally, Section V concludes this article.
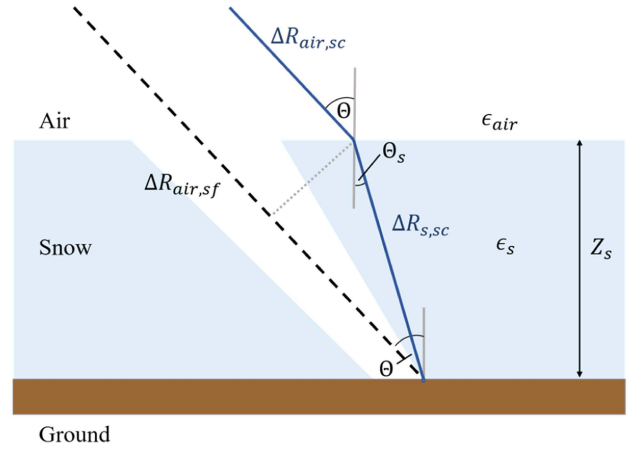

Fig. 1. Refraction of a radar wave in a snow pack. When the ground is covered by snow of the height Z_S, the radar wave travels first the distance $\Delta R_{\mathrm{air,sc}}$ in air and is then refracted in the snow pack, because the dielectric constant of snow ϵ_s is different than the dielectric constant of air $\epsilon_{\mathbf{air}}$. After the distance $\Delta R_{s,\mathrm{sc}}$ it reaches the ground. For snow-free conditions, the radar wave travels the distance $\Delta R_{\mathrm{air,sf}}$.

II. THEORY AND METHODS

A. Relationship DInSAR Phase and SWE Change

The SWE parameter combines the information on snow density ρ_s and snow depth Z_s and refers to the theoretical depth of water which is obtained if the snow pack melted instantaneously. It can be expressed as

$$\mathrm{SWE} = \frac{1}{\rho_w} \int_0^{Z_s} \rho_s(z) \, dz \approx Z_s \rho_s / \rho_w \qquad (1)$$

where ρ_w is the density of water.

The model proposed in [23] for SWE change estimation of dry snow using repeat-pass SAR interferometry is based on a nearly linear relationship between the SWE change and the differential interferometric phase between two SAR acquisitions [22].

The interaction between the radar waves and snow is governed by the dielectric properties of snow. Since snow has a different dielectric constant than air, a radar wave experiences refraction when propagating through a snow layer, as shown in Fig. 1. When comparing the optical path length of the wave for snow-free and snow-covered conditions, a path delay can be observed, which results from the different path length due to refraction in the snow pack and also from the different propagation speed of the radar wave in the snow. This path delay also occurs in the case of a snow depth change ΔZ_s between two measurements and is proportional to ΔZ_s. Such delay translates into a DInSAR phase difference, which can be, in turn, linked to the snow depth change. By considering the geometry in Fig. 1, a nearly linear relationship between the SWE change and the differential interferometric phase between two SAR acquisitions can be obtained. The relation between the interferometric phase difference $\Delta\Phi_\mathrm{s}$ and SWE change $\Delta\mathrm{SWE}$ is then the following [23]:

$$\Delta\Phi_s = 2\,k\frac{\alpha}{2}\left(1.59 + \Theta^{\frac{5}{2}}\right)\Delta\mathrm{SWE} \qquad (2)$$
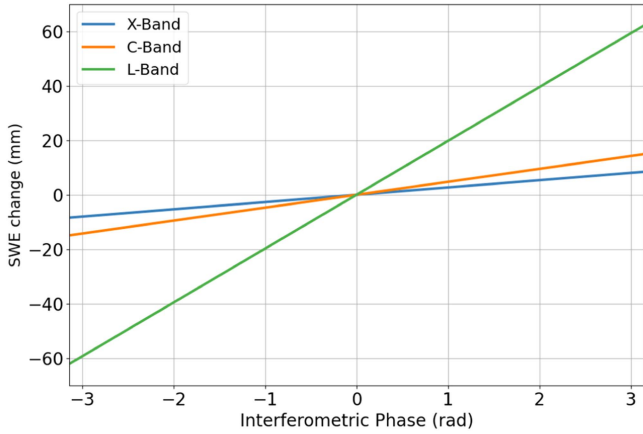
Fig. 2.   SWE change in dependence of the interferometric phase for X-, C-, and L-bands. For a certain SWE change, smaller interferometric phases are measured for longer wavelengths.
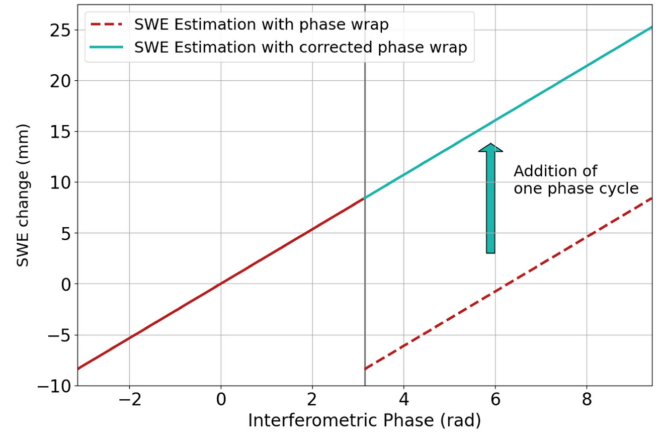

Fig. 3.   SWE change in dependence of the interferometric phase. SWE change values above the phase wrap threshold suffer from phase wraps and will be underestimated (red dotted line), which can be corrected by adding a phase cycle (green line).

where α is a parameter close to 1, which can be adjusted to reduce the root mean square error (RMSE) between the numerical approximation and the exact solution for different snow densities and incidence angles. For snow densities between 0.2 g/cm^3 and 0.4 g/cm^3 and incidence angles between 30° and 40°, α is lying in the range from 0.98 to 1. However, when using a fixed value of $\alpha = 1$, the maximum error for incidence angles smaller than 40° lies below 3% [23].

For dry snow, which is of interest for this study, the absorption is assumed to be negligible and is, therefore, not considered. Furthermore, volume scattering in the snow pack is not considered, as it can be neglected for dry snow and frequencies below 20 GHz [29].

It can be seen in (2) that the interferometric phase difference is positive if the SWE increases between the two acquisitions, due to the linear relation between ΔSWE and $\Delta\Phi_s$.

By rearranging (2), an expression for the SWE change ΔSWE is obtained

$$\Delta\text{SWE} = \frac{\Delta\Phi_s}{k\alpha\left(1.59 + \Theta^{\frac{5}{2}}\right)}. \tag{3}$$

In Fig. 2, ΔSWE is plotted against $\Delta\Phi_s$ for an incidence angle of $\Theta = 34°$ for different frequencies. The used frequencies are: in the X-band, 9.65 GHz; in the C-band, 5.41 GHz; and in the L-band, 1.26 GHz. It can be seen that the ΔSWE estimation has a strong dependence on the wavelength.

Moreover, since the DInSAR phase can only be used to calculate an SWE change between two acquisitions [see (3)], it just allows to monitor the differential SWE over time. The estimation of the total SWE requires a time series of measurements starting at snow-free conditions or an initial guess of SWE and a cumulative sum of the ΔSWE estimates.

B. ΔSWE Estimation Threshold Due to Phase Wrapping

It has to be taken into consideration that only a limited range of ΔSWE can be retrieved unambiguously using (3) since the differential interferometric phase can be only measured in an
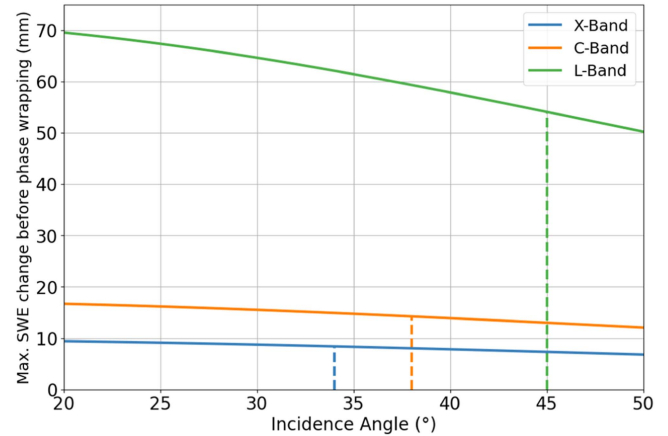

Fig. 4.   SWE change between two acquisitions for a phase difference $\Delta\Phi_s = \pi$ in dependence of the incidence angle for X-, C-, and L-bands. Higher SWE changes suffer from phase wrapping. The equivalent thresholds apply for negative changes. The vertical lines indicate the incidence angles of the satellite data used in this study (blue: TanDEM-X, orange: Sentinel-1, and green: ALOS-2).

interval between $[-\pi, \pi]$. An example for the X-band is shown in Fig. 3 for an incidence angle of $\Theta = 34°$. The solid line represents the interval $[-\pi, \pi]$, which corresponds to a range of SWE changes of $[-8.37$ mm, 8.37 mm$]$. This is the interval that can be estimated unambiguously. For higher ΔSWE, the phase would exceed π. However, in that case, the phase wraps again to $-\pi$. Therefore, the results for ΔSWE values, which would correspond to $\Delta\Phi_s$ values in the interval $[\pi, 3\pi]$, are the same as for the interval $[-\pi, \pi]$. The same occurs when a ΔSWE decrease exceeds the negative threshold of the interval.

The interval, in which ΔSWE values can be retrieved unambiguously, strongly depends on the wavelength and is approximately seven times larger for the L-band than for the X-band. Fig. 4 shows the upper boundary of this ΔSWE interval (before phase wrapping occurs) at X-, C-, and L-bands in dependence of the incidence angle. The interval generally decreases with larger incidence angles as the path length of the radar wave in

the snow pack increases. Because ΔSWE values exceeding this interval result in phase wraps of $\Delta\phi_s$, they need to be detected and compensated for a correct ΔSWE estimation.

C. Ground-Based and Multifrequency DInSAR Phase Correction for ΔSWE Estimations

For the investigation of the phase wrapping issue, ground measurements of ΔSWE are used in this study to correct for phase wraps. It is assumed that the retrieved phase values suffer from phase wrapping errors in cases where the ground-based measurements lie outside the aforementioned interval. The results are then corrected by adding a full phase cycle, as indicated by the green line in Fig. 3. This enables the retrieval of ΔSWE values outside of $[-\pi, \pi]$. The ground measurements also may contain measurement errors. Therefore, for ground measurements within $+/-5\%$ of the boundary of the interval, it is checked whether a phase wrap correction needs to be applied in order to improve the results.

Another way to correct the phase wraps is a multifrequency approach, exploiting the fact that long wavelength measurements are less affected by phase wraps. In this study, ΔSWE estimates from SAR acquisitions with a longer wavelength (e.g., ALOS-2) are used to correct the ΔSWE estimates from shorter wavelength data (e.g., Sentinel-1). If the acquisitions are acquired at different dates, the SWE change estimates from the longer wavelength are linearly interpolated between the measurement dates. Phase wraps of the shorter wavelength data are corrected as follows. When the SWE change estimates including the standard deviation of the longer wavelength measurements are below the phase wrap threshold, no correction is performed. In the case that the threshold lies within the standard deviation of the SWE change estimate of the longer wavelength, it is calculated if adding a phase cycle decreases the difference between the SWE change estimates of the two frequencies. If so, a phase cycle is added. In the case that the SWE change estimate including the standard deviation lies above the threshold, a phase cycle is added.

D. ΔSWE Deviation Due to Phase Standard Deviation in Dependence of the Coherence

The interferometric phase is estimated from N interferogram samples to reduce phase noise. The probability density function pdf of the phase Φ is given by [30]

$$\text{pdf}\,(\Phi, N)$$
$$= \frac{\Gamma\left(N + \frac{1}{2}\right)\left(1 - |\gamma|^2\right)^N |\gamma| \cos\left(\Phi - \Phi_0\right)}{2\sqrt{\pi}\Gamma\left(N\right)\left(1 - |\gamma|^2\cos^2\left(\Phi - \Phi_0\right)\right)^{N+\frac{1}{2}}}$$
$$+ \frac{\left(1 - |\gamma|^2\right)^N}{2\pi} 2F_1\left(N, 1, \frac{1}{2}|\gamma|^2\cos^2\left(\Phi - \Phi_0\right)\right) \quad (4)$$

where γ is the complex coherence (see Section III-C). The pdf is used to calculate the standard deviation of the phase in dependence of the coherence for different numbers of samples (i.e., looks). As can be seen in Fig. 5, the phase standard deviation significantly decreases for a higher number of samples.
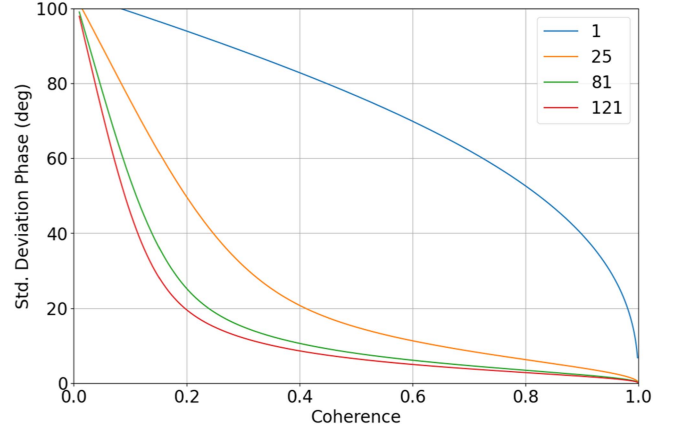

Fig. 5. Standard deviation of the phase in dependence of the coherence for $N = 1; 25; 81;$ and 121 samples. It can be observed, that the standard deviation decreases for higher coherence values and larger number of looks.
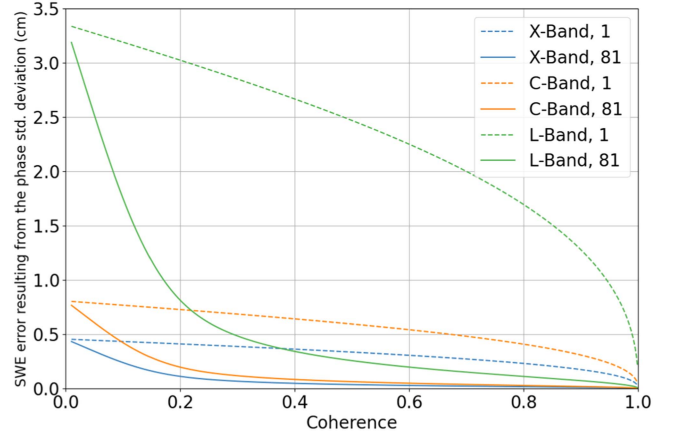

Fig. 6. ΔSWE error resulting from the standard deviation of the phase for X-, C-, and L-bands. For each band, the results for 1 and for 81 samples in a multilook window are compared. The obtained ΔSWE error is proportional to the frequency.

Since the SWE change is calculated using the interferometric phase, the phase standard deviation can be converted into a ΔSWE estimation error with (3). The ΔSWE estimation errors for different frequencies are displayed in Fig. 6 for 1 and 81 looks. Since the error is proportional to the frequency, the ΔSWE estimation error is higher for the L-band than for the X-band.

III. EXPERIMENTAL DATA

A. SAR Data

A list of the utilized SAR data can be found in Table I.

The TanDEM-X (TDX) dataset contains a time series for the winter 2010–2011 acquired in strip map mode. X-band data in VV and VH polarizations are available with a temporal baseline of 11 days. The incidence angle is 34°.

To investigate C-band, Sentinel-1 data were chosen for the winter 2019–2020. Because there were two polar orbiting satellites, a repeat-pass time of 6 days can be achieved. The polarizations are VV and VH, with an incidence angle of 38°.

Satellite (frequency)	Dates		Incidence angle	Channel	Applied Multilook (rgxaz)
TDX (9.65 GHz)	2010-10-25 – 2011-03-17	Every 11 days	34°	VV, VH	9x9
Sentinel-1 (5.41 GHz)	2019-11-06 – 2020-03-17	Every 6 days	38°	VV, VH	7x3
ALOS-2 (1.26 GHz)	2019-12-30 – 2020-03-21	Every 14 days	45°	HH, HV	5x5

Fig. 7. Snow scale that measures the SWE of the snow pack at the IOA [31] with location on the map. The accumulated snow is weighted over the center plate.

Additionally, ALOS-2 acquisitions in the L-band are also available from the winter 2019–2020 with a temporal resolution of 14 days. HH and HV were acquired with an incidence angle of 45°.

Here, it has to be considered that due to data availability, the X-band data were acquired 9 years before the C- and L-bands data. However, the months that are covered are similar. Furthermore, due to the higher backscatter and coherence, the co-pol channel, either VV or HH, was used in this study.

B. Ground Data and Test Site

The Arctic Space Observation Centre lies close to the city of Sodankylae in northern Finland; see Fig. 7. The intensive observation area (IOA; N67.36183, E26.63415) is a test site where ground measurements are performed. It is located in a forest opening that is surrounded by a pine forest with about 15-m high trees. The area is flat and lies approximately 175 m above sea level.

In the winter 2010–2011, manual measurements of snow properties, like SWE, depth and temperature were performed at the IOA. The measurement dates are not more than 3 days apart from the satellite acquisitions, and are therefore used for the validation of the satellite data.

Since 2015, daily automated SWE measurements [31] have been performed using a snow scale at the IOA, where the snow accumulation is weighted over a center panel (see Fig. 7). Weather parameters (i.e., temperature, snow depth, and wind speed) are provided by an automated weather station (AWS) [32].

C. Interferometric Processing

The satellite radar data are processed using the TanDEM-X Interferometric processor (TAXI) by German Aerospace Center [33], which is adapted to ALOS-2 and Sentinel-1, for which the InSAR processing is performed on a burst by burst basis. For all satellites, the reference and secondary images were geometrically coregistered by using a DEM and orbit information, common band filtering was applied and the flat earth phase was compensated.

The complex coherence γ is calculated between two nearest-neighbor (consecutive) acquisitions, either for the VV or for the HH channel, with the shortest temporal baseline possible, using the cross correlation of both signals with

$$\gamma = \frac{\langle s_1 s_2^* \rangle}{\sqrt{\langle s_1 s_1^* \rangle \langle s_2 s_2^* \rangle}} \tag{5}$$

where s_1 and s_2 are the signals of the reference and secondary images, respectively, and $\langle \ldots \rangle$ represents the expectation value. Appropriate multilooking is required to achieve sufficient theoretical ΔSWE estimation performance (see Section II-D). The multilooking windows for the different frequencies can be found in Table I and are adapted to match the forest opening of the IOA.

One example of the L-band HH interferometric coherence $|\gamma|$ is shown in Fig. 8(a) for the image pair of the 09.03.2020 and 23.03.2020. Particularly low coherence values correspond to lakes and rivers. Fig. 8(b) shows a zoom in to the test site marked with green. In general, coherences are rather low, showing the challenging DInSAR scenario due to the large temporal baselines.

The interferometric phase is calculated from the coherence between the two acquisitions and the flat earth phase is removed. To obtain only the phase contribution from the snow pack, any atmospheric phase contributions have to be removed. This is achieved by a phase calibration at a stable scatterer in the vicinity of the test site. Due to the lack of proper calibration targets, a stable scatterer is identified by finding a resolution cell with particular high and temporally stable backscatter and coherence. The high coherence of the stable scatterer, corresponding to buildings, and its location near the test site is marked in red in Fig. 8(b) for an L-band example. More sophisticated atmospheric phase calibration methods, like, for example, [34] and [35], were investigated but failed due to the generally low coherence in the data.

IV. RESULTS

A. ΔSWE Estimation X-Band

The temperature and SWE data are displayed in Fig. 9 for the dates of the TDX acquisitions. Except for the first acquisition
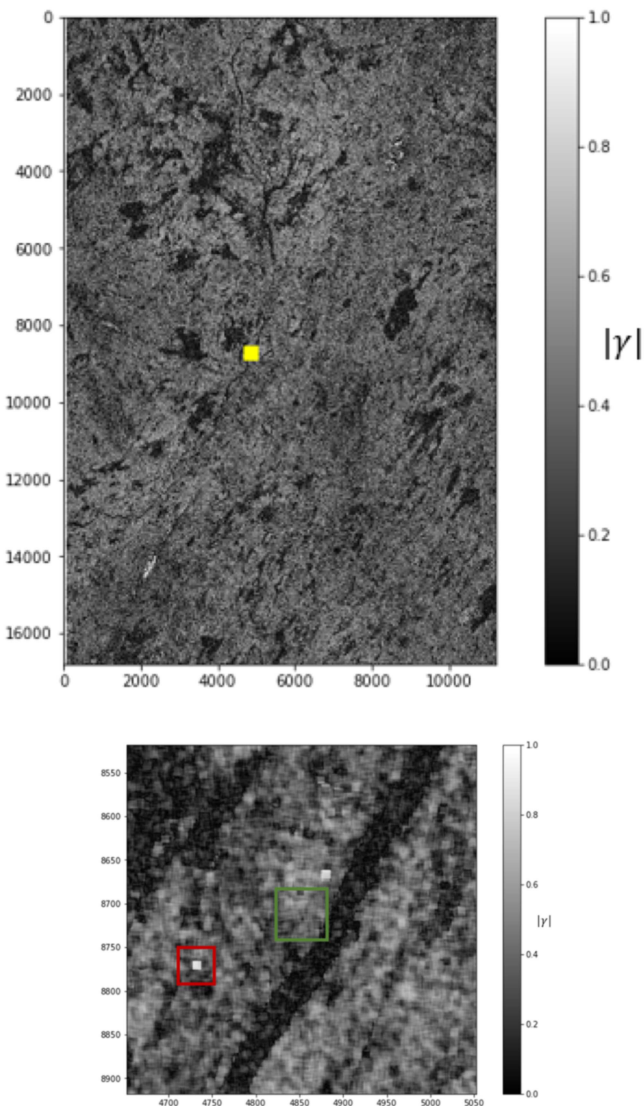
Fig. 8. Coherence of the HH channel for the L-band acquisition on the 09.03.2020/23.03.2020 in range and azimuth coordinates. (a) For the total SAR scene. The area of the test site is marked in yellow. (b) Zoom in to the test site. The test site and the calibration point are marked with green and red, respectively.

date, the temperature was below zero degrees and the SWE was increasing.

The time series of the coherence for the VV channel over the test site is displayed in Fig. 10. It shows that the coherences are rather small, but are especially low between the 19.12.2010 and 30.12.2010 and between the 30.12.2010 and 10.01.2010 reaching values below 0.2. The comparison with the ground measurements (see Fig. 9) reveals that for these measurements especially high temperature gradients were encountered. Including the only negative SWE change in the time series, this might explain the small coherences as a larger change in snow structure can be expected [36].

After calculating the coherence and the interferometric phase, (3) is applied for the ΔSWE estimation. Fig. 11(a) shows the ΔSWE ground measurements and the DInSAR-retrieved SWE changes between the acquisition dates. Since only SWE differences between two acquisitions can be retrieved from the

Fig. 9. (a) Air temperature and (b) total SWE measurements at the TanDEM-X acquisition dates.
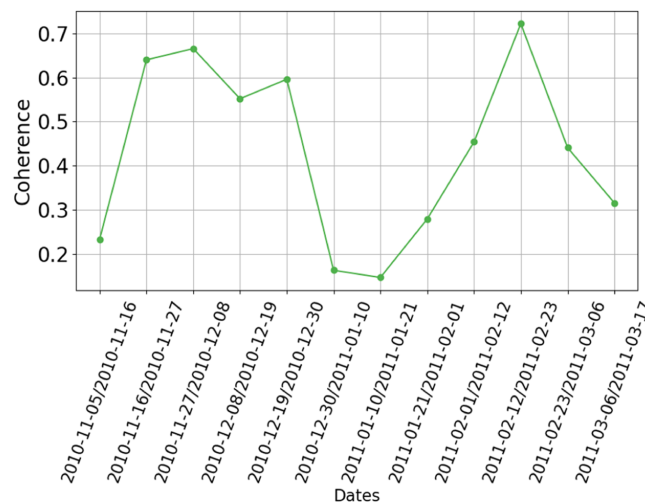

Fig. 10. Coherence for the X-band data. In the x-axis labels, the first date represents the reference acquisition and the second date the secondary acquisition of the interferogram.

ΔSWE estimation model, the values would have to be added over time to obtain a total SWE. However, a large discrepancy between the retrieved and measured SWE changes can be observed with an RMSE before the correction of phase wraps of $\text{RMSE}_{b,X} = 13.12$ mm.

As mentioned, since the DInSAR phase lies in a range between $[-\pi, \pi]$, SWE differences outside this interval cannot be retrieved from the satellite data due to phase wrapping. For the used frequency and incidence angle that interval corresponds to a SWE change in the range of $[-8.37$ mm, 8.37 mm]. The upper boundary is marked with a blue vertical line in Fig. 4. After
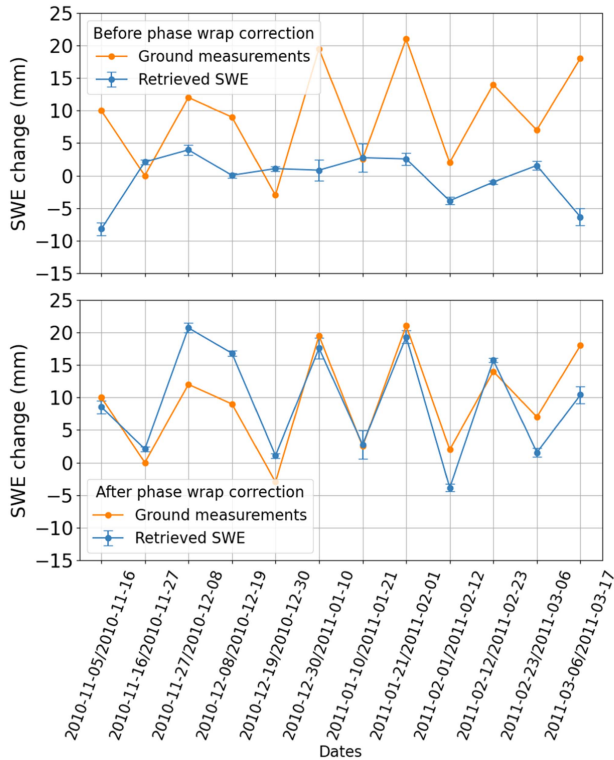
Fig. 11. Ground measured and from X-band data retrieved SWE change values. (a) Before phase wrap correction. (b) After phase wrap correction using the ground measurements.
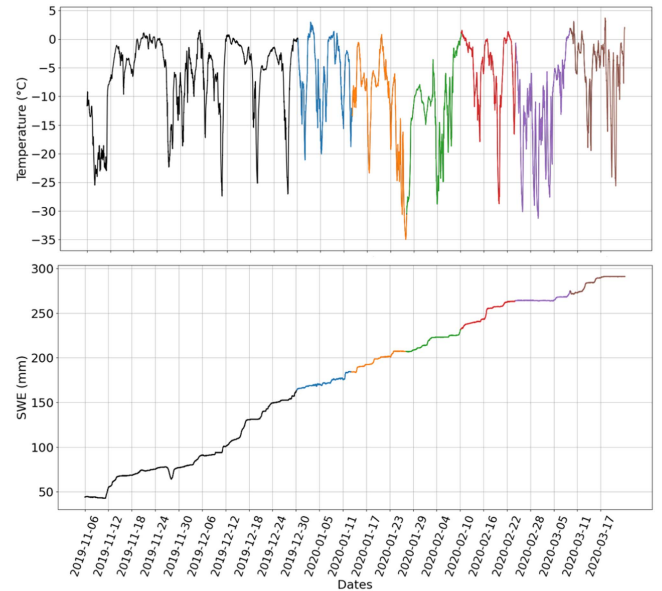

Fig. 12. (a) Air temperature and (b) total SWE measurements. The vertical grid lines correspond to the Sentinel-1 acquisitions. The colors mark the 14 days temporal baseline between the ALOS-2 acquisitions.
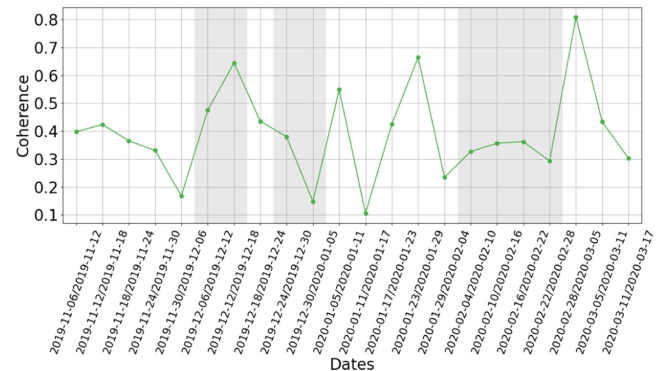

Fig. 13. Coherence for the C-band data. In the x-axis labels, the first date represents the reference acquisition and the second date the secondary acquisition of the interferogram. The gray background marks the measurements where the temperature was above zero degrees either at the first or second acquisition of the interferogram.

using the ground measurements to detect phase wraps and to correct these by adding the appropriate amount of phase cycles, the ΔSWE estimations displayed in Fig. 11(b) are obtained, showing a better correlation between the measured and retrieved ΔSWE values with an RMSE after correction of $\text{RMSE}_{a,X} = 4.92$ mm. There are some discrepancies, but the general trend is well represented with the retrieved and corrected ΔSWE values. Since the phase wrap correction has a big impact on the results particularly for short wavelengths, we calculated the RMSE relative to a full phase cycle (i.e., the ΔSWE change which corresponds to 2π phase) to have a better comparison between frequencies, which is discussed in Section IV-D. Without the phase wrap correction, it is not possible to retrieve the SWE change correctly in this case because the ground measurements show that the threshold for phase wraps is often exceeded. Therefore, it is important to correct for phase wraps when performing the ΔSWE retrieval using DInSAR X-band data with a temporal baseline of 11 days.

B. ΔSWE Estimation C-Band

In Fig. 12, the temperature and the total amount of SWE for the winter 2019–2020 are displayed. The vertical grid lines represent the 6 days between the Sentinel-1 acquisitions. Overall it can be seen, that for both investigated winters in this study, the SWE is almost steadily increasing, but especially in the 2019–2020 winter, the temperatures were sometimes above zero degrees.

The coherences for the VV polarized C-band data are displayed in Fig. 13. In many cases, the coherences are very low.

The coherences can be compared to the temperature data in Fig. 12. It can be seen that in many cases, the air temperature rises above zero degrees likely resulting in snowmelt, which causes the low coherences. The gray background colors mark the measurements where the temperature was above zero degrees either at the first or second acquisition of the interferogram. However, the coherence can also decrease if the temperature was above zero degrees between the acquisitions and the snow pack refroze again, resulting in a refrozen melt layer, which might contribute to the backscattering, and thus, bias the ΔSWE retrieval. This may have been the cause for the low coherence 30.11.2019/06.12.2019.

The ΔSWE retrieval is also applied to the interferometric phase of the Sentinel-1 acquisitions. Note that in this case, the investigated winter is 2019–2020, and thus, differs from the X-band estimations.
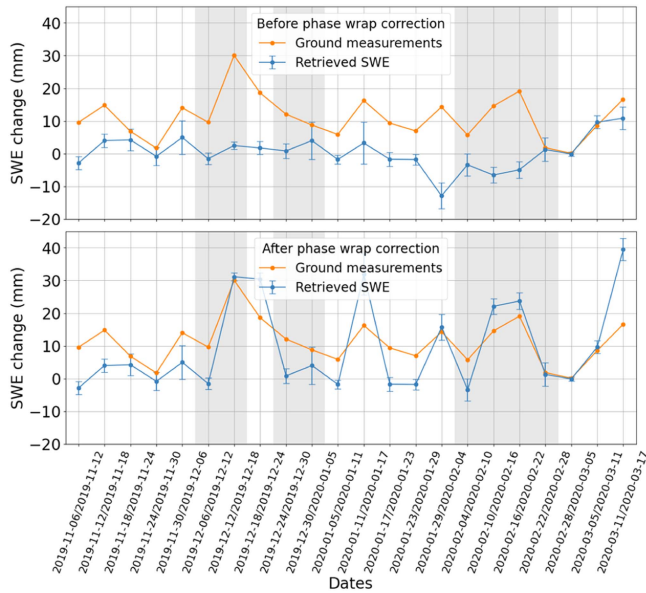
Fig. 14. Ground measured and from C-band data retrieved SWE change values. (a) Before phase wrap correction. (b) After phase wrap correction using the ground measurements. The gray background marks the measurements where the temperature was above zero degrees either at the first or second acquisition of the interferogram.

The interval in which the SWE change can be retrieved unambiguously is $[-14.32 \text{ mm}, 14.32 \text{ mm}]$ (orange vertical line in Fig. 4). Fig. 14(a) shows the SWE differences for temporal baselines of 6 days with an RMSE before correction of $\text{RMSE}_{b,C} = 13.47$ mm. Also here, the ground-measured SWE changes often exceed the phase wrap threshold, and therefore, the missing phase cycles need to be corrected. The obtained results are displayed in Fig. 14(b). The RMSE between the ground measurements and retrieved SWE changes is $\text{RMSE}_{a,C} = 9.46$ mm after correction. Although some similarities can be observed for the general trend, in many cases, the discrepancy is very high. A possible reason here may be again large temperature gradients, as, for example, on the 18.12.2019 /24.12.2019 or the 23.01.2020/29.01.2020 when a larger snow structure change can be expected, which can have a not yet fully understood effect on the phase [24]. Another possible reason for that might be the positive temperature that occurred many times throughout the time series. This causes not only low coherences, resulting in large phase standard deviations, and thus, ΔSWE estimation errors, but also in potential systematic errors. Due to the resulting snowmelt, the radar wave will get attenuated in the snow pack [37] and is not able to penetrate to the ground when the temperature is above zero degrees at the acquisition time. This may be the reason for the following discrepancies: for the underestimations, because less snow is propagated by the radar wave, but it might be also seen as an overestimation in the plot, in case where the snow was significantly underestimated and the measured phase is, therefore, one phase cycle off. This shows that the selected winter season, which was chosen due to its coincidence with the available ALOS-2 data, was not optimal due to the weather conditions. However, it is also clear that the phase wrapping issue plays an important role in the ΔSWE estimations using C-band
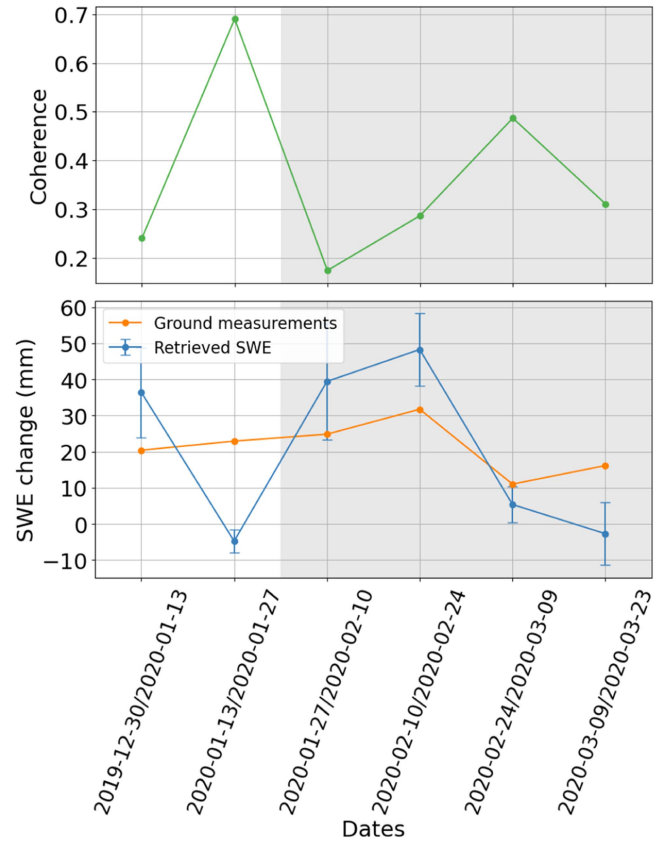

Fig. 15. (a) Coherence for the L-band data. In the x-axis labels, the first date represents the reference acquisition and the second date the secondary acquisition of the interferogram. (b) Ground measured and from L-band data retrieved SWE change values. The gray background marks the measurements where the temperature was above zero degrees either at the first or second acquisition of the interferogram.

data with a temporal baseline of 6 days. Nonetheless, some general trends can be represented with the retrieved SWE change.

C. ΔSWE Estimation L-Band

The ground measurements for the ALOS-2 acquisitions are also displayed in Fig. 12, which cover roughly the second half of the temporal coverage of Sentinel-1. The colors mark the 14 days temporal baseline between the dates of the ALOS-2 acquisitions.

Fig. 15(a) shows the ALOS-2 L-band coherences in the HH polarization. The coherences are often very low over the test site. Here, the same winter as for C-band was investigated. As it can be seen in Fig. 12, the temperatures at the acquisition times were often above zero degrees, causing low coherences as a result of snowmelt.

For the ALOS-2 wavelength and incidence angle, the calculated threshold for phase wrapping is outside the interval of $[-54.4 \text{ mm}, 54.4 \text{ mm}]$. This is always larger than the ground measured SWE changes. Therefore, phase wrap corrections do not have to be considered for the L-band data. The results for the ΔSWE retrieval are shown in Fig. 15(b) with the RMSE between the retrieved and measured SWE change being $\text{RMSE}_{b,L} = 17.76$ mm. Since it is the same winter as for the C-band

measurements, the temperatures above zero degrees (see Fig. 12) are a problem again. The general trend can be represented, but especially the second measurement point has a high discrepancy between the estimated ΔSWE from the ALOS-2 data and the ground measurements and the discrepancy is even higher than for the following interferograms, where the coherence was lower and the temperature higher. For this point, the temperature decreases by 35 °C in the week before the second acquisition after being shortly above zero degrees. This high temperature gradient may have some influence on the snow structure. In [24], a decorrelation was observed for high temperature gradients, which may also be linked to changes in the snow properties. However, these effects need to be analyzed more, since this ALOS-2 interferogram has an unusually high coherence. Even if the snow cover can be seen as an isolating layer, high temperature changes may also have an influence on the ground. Since L-band measurements are also able to penetrate into frozen ground [38], this might also affect the interferometric phase.

D. Comparison of ΔSWE Estimation From Different Frequencies

The results of the different frequencies are compared directly in a scatter plot showing every SWE change estimation. Fig. 16(a) shows the estimated SWE changes compared to the ground measured values before phase wrap correction. Many points are underestimated, especially for the small wavelengths of X- and C-bands. This results from the smaller nonambiguous phase interval of retrievable SWE changes for shorter wavelengths.

After phase wrap correction, the results in Fig. 16(b) are obtained. The highest improvement can be observed for X-band. This underlines the fact that, for X-band SAR measurements, phase wraps of the interferometric phase after an SWE increase are important to correct for the used temporal baseline. For the X-band, the phase wrap correction has a large impact compared to the relatively small interval of unambiguous ΔSWE estimates. Nevertheless, the small wavelengths can contribute to higher ΔSWE estimation accuracies than larger wavelengths, but are rather only applicable for shorter temporal baselines or in a multifrequency approach (see Section IV-F). For the C-band, the points where the phase wraps were corrected according to the ground measurements are now slightly overestimated. In the case of the L-band measurements, no phase wrap correction was necessary. Even though one clear outlier can be observed at the L-band, related to strong temperature changes, other points represent well the general trend. In order to allow for a better comparison between the frequencies, for each frequency, a relative RMSE (RMSE$_{rel}$) is calculated, by setting the RMSE after correction in relation to the 2π phase cycle interval (ΔSWE$_{2\pi\_Interval}$) with

$$\text{RMSE}_{rel} = \text{RMSE}_a / \Delta\text{SWE}_{2\pi\_\text{Interval}} \qquad (6)$$

shown in Table II. The performance of the L-band retrieval shows a smaller RMSE$_{rel}$ compared to the X- and C-bands results, meaning that here the retrieval performed the best in
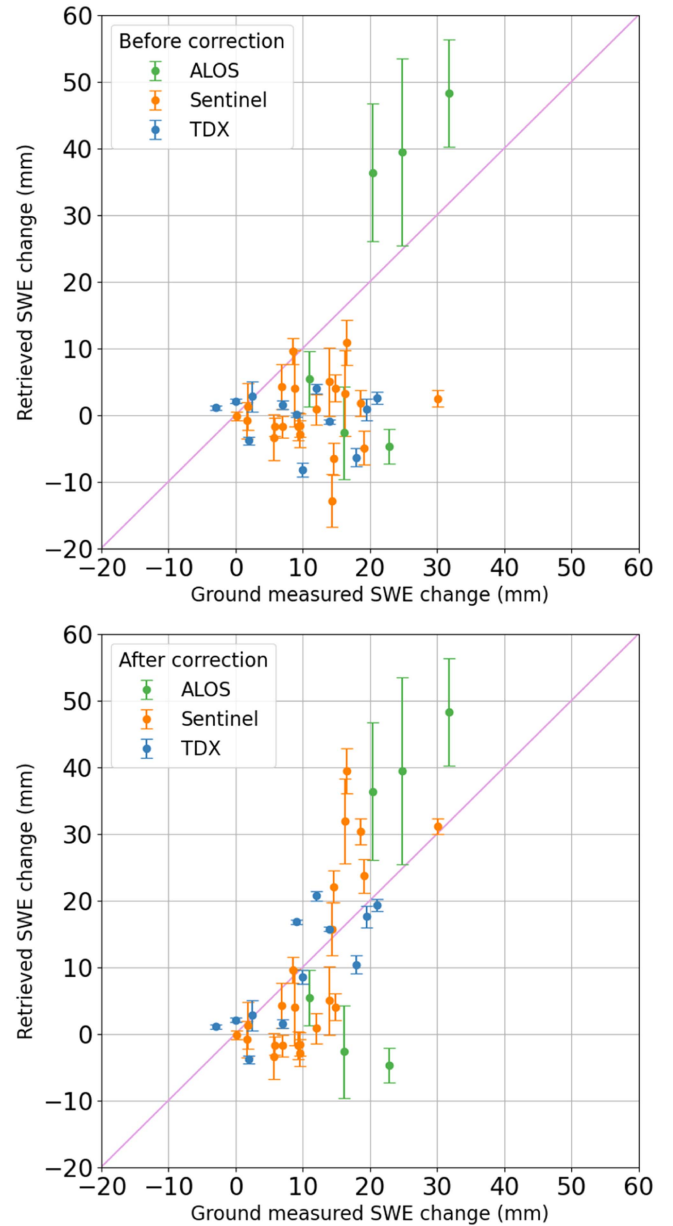

Fig. 16. Scatter plot of the retrieved SWE changes compared to the ground measured SWE changes for X-, C-, and L-bands. (a) Before correcting the phase wraps based. (b) After correcting the phase wraps based on the ground measurements.

TABLE II
RMSE PHASE WRAP CORRECTION FROM GROUND MEASUREMENTS

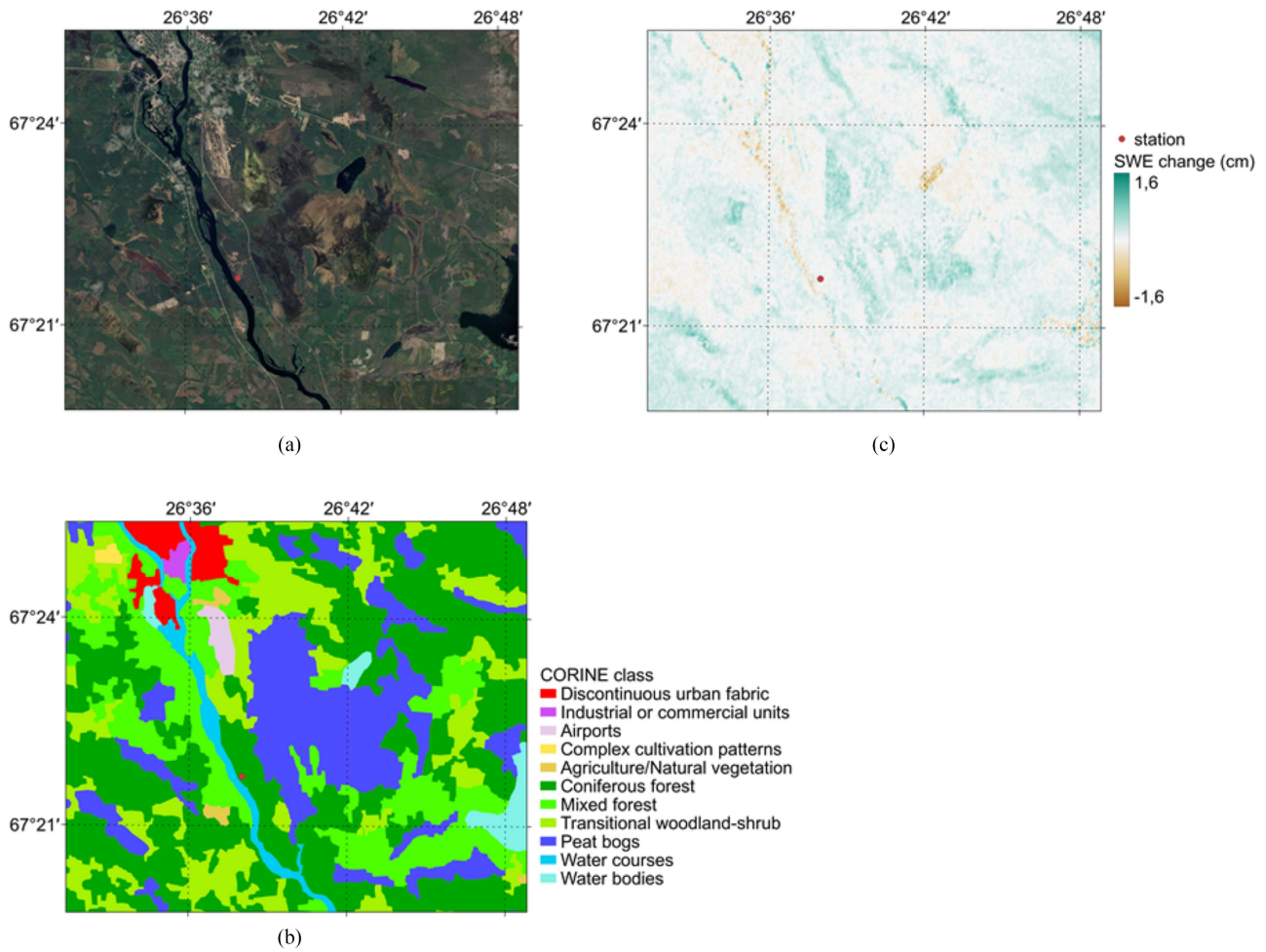| Frequency	X band	C band	L band
RMSE$_b$ (mm)	13.12	13.47	17.76
RMSE$_a$ (mm)	4.92	9.46	17.76
RMSE$_{rel}$	0.29	0.33	0.16

Fig. 17. Map of the area around the station. (a) Optical image. (b) CORINE landcover classes. (c) SWE change map from Sentinel-1 using the 28.02.2020/05.03.2020 interferogram. The red dot marks the location of the test site.

relation to the phase wrap interval. The individual errors after correction are however smaller for shorter wavelengths. Therefore, the sensitivity to retrieve smaller changes is higher for smaller wavelengths, even though the overall results are better for longer wavelengths. Note here, that this comparison is not optimal, as different temporal baselines and different winters are compared.

Across all frequencies, it can be observed in Fig. 16(b) that smaller SWE changes are mostly underestimated, while higher SWE changes are mostly overestimated. A factor influencing the ΔSWE retrieval is the phase calibration (see Section III-C). Since the reference point is not ideal, a random error in the phase calibration could have been induced. Furthermore, as it is not known whether the stable point was covered by snow or not, the reference phase might contain some signal delay due to snow. When calibrating the phase over the test site according to this reference, an underestimation can be expected. However, this disagrees with the overestimations for higher SWE changes. A reason for the general differences is the likely wet snow in C- and L-bands, resulting in discrepancies between the estimated and measured SWE changes (see Section IV-B).

E. Spatial C-Band ΔSWE Estimation

For an assessment of the spatially distributed ΔSWE retrieval, with the potential for high spatial resolution and large-scale coverage with spaceborne SAR, the SWE change is estimated in the area around the in situ station. Fig. 17(a) shows an optical true-color image of the area and Fig. 17(b) displays the CORINE landcover information [39]. The area is mostly covered with forest and peat bogs, while the urban areas in the north belong to the town of Sodankylae. Fig. 17(c) displays the corresponding SWE change map of the area calculated from the Sentinel-1 interferogram between 28.03.2020 and 05.03.2020. During this timeframe, the SWE remained stable at the in situ station. In the ΔSWE map, inland water bodies appear noisy as expected due to temporal decorrelation. Close to the in situ station, almost no SWE change is measured, which is in accordance with the ground measurements. The large peat bog in the center of the study area shows a noticeable positive ΔSWE. This may be due to the lower terrain that favors snow accumulation due to wind effects. However, the phase signal that is measured might not only result from the SWE change, but also from the
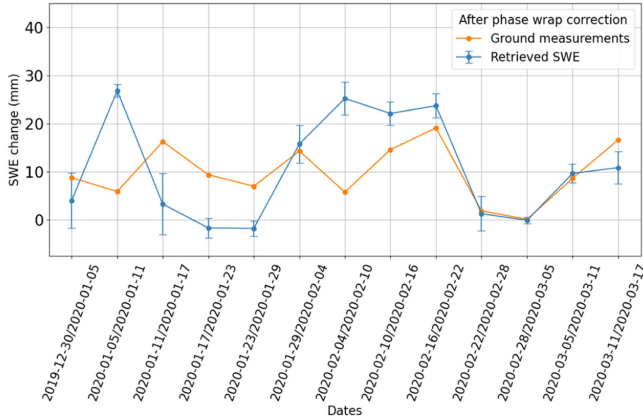
Fig. 18. Ground measured and from C-band data retrieved SWE change values. The phase wraps are corrected with the L-band SWE estimations.

TABLE III
RMSE MULTIFREQUENCY PHASE WRAP CORRECTION

Frequency	C band
$RMSE_{b,multi,C}$ (mm)	13.38
$RMSE_{a,multi,C}$ (mm)	10.09
$RMSE_{a,groundC}$ (mm)	9.66

properties of the bogs. In the urban areas of Sodankylae, the SWE change has a tendency toward negative SWE change values with some variations. This may be the result from small-scale local SWE changes caused by anthropogenic structures. Further investigation is needed to analyze the influence of different land cover on the SWE change retrieval.

F. Multifrequency Phase Wrap Correction

Previously, ground measurements were used to correct the phase wraps of ΔSWE estimations in the X-band (see Section IV-A) and C-band (see Section IV-B), as they suffer from phase wraps if the SWE change exceeds a certain threshold.

However, the goal is to correct the ΔSWE estimations without requiring ground measurements. This can be achieved using a multifrequency approach. In this study, the L-band data (see Section IV-C) are not affected by phase wraps because of its long wavelength. As the L- and C-bands data were acquired in the same winter, L-band ΔSWE estimates are used to detect and correct phase wraps in the C-band data. Due to the different acquisition dates and temporal baselines for the ALOS-2 and Sentinel-1 images, the retrieved SWE changes from ALOS-2 are linearly interpolated between the measurement dates. Fig. 12(b) shows that it is reasonable to assume a linear SWE change. Then, the interpolated SWE change from the L-band measurements is used to detect where a phase cycle needs to be added to the C-band ΔSWE estimations. By correcting the C-band values accordingly, the results in Fig. 18 are obtained with an RMSE after multifrequency phase wrap correction of $RMSE_{a,\mathrm{multi},C}$ = 10.09 mm, while the RMSE before correction for this interval was $RMSE_{b,\mathrm{multi},C}$ = 13.38 mm, which is the same as the single frequency $RMSE_{b,C}$ result, but only for the time span covered by the L-band data. Here, discrepancies can be observed with some clear overestimations in the middle of the time series, which are related to the L-band overestimations in Fig. 15. However, the error is only slightly larger than for the ground-based corrected C-band results in Fig. 14(b), which is $RMSE_{a,\mathrm{ground}\,C,}$ = 9.66 mm, summarized in Table III. When comparing the ΔSWE results after phase wrap corrections from the multifrequency approach and the one from the ground measurements, seen in Fig. 14(b), 9 of the 13 ΔSWE estimates utilized for the

multifrequency approach were corrected or not corrected in the same way. Furthermore, it has to be taken into consideration that the investigated winter was not optimal due to high temperatures and low coherences. However, this shows that L-band ΔSWE estimates can be used to correct phase wraps in smaller wavelength SAR measurements like C-band, because the L-band measurements are less likely to suffer from phase wraps. Even though the performance of this approach was not yet completely satisfying, due to the discrepancy of the L-band data to the ground measurements, this method is promising, because it enables the phase wraps correction without the need of additional ground measurements. This is essential for future large-scale space borne applications. Unfortunately, no winter exists where all three frequencies were acquired contemporaneously.

V. CONCLUSION

The SWE change is retrieved using the DInSAR phase difference for X-, C-, and L-bands. Since the interferometric phase lies in an interval between $[-\pi, \pi]$, only a range of SWE change values can be retrieved unambiguously. For larger changes of SWE, phase wraps occur. To investigate the effect of the phase wrap errors, they are corrected with ground measurements in this study. Furthermore, a multifrequency approach is presented to overcome the necessity of ground measurements, which could pave the way toward a DInSAR SWE information product with spaceborne SAR.

At the X-band, the main limitation for the ΔSWE retrieval is the phase wrapping of the measured interferometric phase. Because of the short wavelength, the interval where the SWE change can be retrieved unambiguously is smaller compared to longer wavelengths, such as L-band. This could be potentially overcome by using temporal baselines much shorter than 11 days in order to reduce the observed SWE change and in turn to minimize the occurrence of phase wraps.

For the C-band, with a temporal baseline of 6 days, the phase cycles also needed to be corrected, which improved the results. However, the remaining discrepancies result most likely from several short melt events during the observed winter.

When using L-band SAR data with a 14 days temporal baseline, the correction for lost phase cycles was not necessary, because the SWE change did not exceed the phase wrapping threshold. Here, the same winter was analyzed as for the C-band data, confirming the possible influence of high temperature gradients and melt events. Moreover, only a short time series was available, limiting the performance assessment. However,

except for one distinct outlier, the general ΔSWE trend was reproduced by the L-band data.

Thus, when choosing a suitable frequency for ΔSWE estimations, it has to be considered that longer wavelengths can monitor higher SWE changes without the need to correct for phase cycles. However, if the phase wraps can be corrected, the ΔSWE estimation is more accurate at shorter wavelengths. This highlights the potential of multifrequency approaches.

In future studies, it would be advantageous to take simultaneous measurements at different frequencies, ensuring same weather and snow conditions. Also, identical temporal baselines between the measurements would increase the comparability of the results. Moreover, the choice of the test site is also very important. In this case, the test site was a small opening located in a forested area. Therefore, some trees in the multilooking window might have affected the resulting ΔSWE retrievals. Furthermore, also the weather conditions play an essential role. Here, especially in the winter analyzed in C- and L-bands, the temperatures often exceeded zero degrees. This may have led to wet snow. Since the method relies on the fact that the radar wave propagates through the whole snow pack and wet snow may cause attenuation of the radar wave, this affects the estimation results. Therefore, areas with stable weather conditions below zero degrees would be preferable. The calibration of the interferometric phase also plays a crucial role for the ΔSWE estimation. In this study, a stable scatterer was found close to the test site. However, even if this stable scatterer had the highest backscatter and coherence in this region, it is not guaranteed that it was not covered by snow during the acquisition, which would also induce an effect on the interferometric phase. Therefore, a corner reflector close to the test field from which snow is regularly removed would be of advantage. Thinking about future spaceborne SAR applications, the phase calibration might be one of the most challenging points.

This study demonstrated the potential and limitations of SAR acquisitions with different frequencies to estimate SWE changes using the DInSAR phase. A promising multifrequency approach is presented to overcome some of the limitations. It combines ΔSWE estimates from two frequencies to correct the phase wraps without the need of ground measurements. This is particularly of interest for upcoming multifrequency SAR missions, like the dual-frequency L- and S-band NASA-ISRO SAR (NISAR) mission [40]. Another possibility will be the combination of Sentinel-1 with ROSE-L [41], allowing the combination of C- and L-bands measurements. Further favorable aspects of ROSE-L and Sentinel-1 are the identical orbits and repeat-pass intervals and a short time interval between their acquisitions. These missions will enable the potential of multifrequency approaches for the estimation of SWE changes, exploiting the high sensitivity of high frequencies with the large nonambiguous phase interval of smaller frequencies.

REFERENCES

[1] J. Cohen, "Snow cover and climate," *Weather*, vol. 49, no. 5, pp. 150–156, May 1994, doi: 10.1002/j.1477-8696.1994.tb05997.x.
[2] S. Rahmstorf, "A new view on sea level rise," *Nature Climate Change*, vol. 1, no. 1004, pp. 44–45, Apr. 2010, doi: 10.1038/climate.2010.29.
[3] H.-O. Pförtner et al., *Climate Change 2022: Impacts, Adaptation, and Vulnerability. Contribution of Working Group II to the Sixth Assessment Report of the Intergovernmental Panel on Climate Change*. Cambridge, U.K.: Cambridge Univ. Press., 2022, doi: 10.1017/9781009325844.
[4] T. P. Barnett, J. C. Adam, and D. P. Lettenmaier, "Potential impacts of a warming climate on water availability in snow-dominated regions," *Nature*, vol. 438, no. 7066, pp. 303–309, Nov. 2005, doi: 10.1038/nature04141.
[5] S. Jörg-Hess, N. Griessinger, and M. Zappa, "Probabilistic forecasts of snow water equivalent and runoff in mountainous areas∗," *J. Hydrometeorol.*, vol. 16, no. 5, pp. 2169–2186, Oct. 2015, doi: 10.1175/JHM-D-14-0193.1.
[6] J. C. Comiso, "Satellite remote sensing of the Polar Oceans," *J. Mar. Syst.*, vol. 2, no. 3/4, pp. 395–434, Aug. 1991, doi: 10.1016/0924-7963(91)90044-U.
[7] A. Bartsch, J. Jansa, M. Schoner, and W. Wagner, "Monitoring of spring snowmelt with Envisat ASAR WS in the Eastern Alps by combination of ascending and descending orbits," in *Proc. Envisat Symp.*, 2007, pp. 23–27.
[8] R. Kelly, "The AMSR-E snow depth algorithm: Description and initial results," *J. Remote Sens. Soc. Jpn.*, vol. 29, no. 1, pp. 307–317, 2009.
[9] M. Takala et al., "Estimating northern hemisphere snow water equivalent for climate research through assimilation of space-borne radiometer data and ground-based measurements," *Remote Sens. Environ.*, vol. 115, no. 12, pp. 3517–3529, Dec. 2011, doi: 10.1016/j.rse.2011.08.014.
[10] R. L. Armstrong, A. Chang, A. Rango, and E. Josberger, "Snow depths and grain-size relationships with relevance for passive microwave studies," *Ann. Glaciol.*, vol. 17, pp. 171–176, 1993, doi: 10.3189/S0260305500012799.
[11] B. J. Vander Jagt, M. T. Durand, S. A. Margulis, E. J. Kim, and N. P. Molotch, "The effect of spatial variability on the sensitivity of passive microwave measurements to snow water equivalent," *Remote Sens. Environ.*, vol. 136, pp. 163–179, Sep. 2013, doi: 10.1016/j.rse.2013.05.002.
[12] D. Li, M. Durand, and S. A. Margulis, "Potential for hydrologic characterization of deep mountain snowpack via passive microwave remote sensing in the Kern River basin, Sierra Nevada, USA," *Remote Sens. Environ.*, vol. 125, pp. 34–48, Oct. 2012, doi: 10.1016/j.rse.2012.06.027.
[13] A. Moreira, P. Prats-Iraola, M. Younis, G. Krieger, I. Hajnsek, and K. P. Papathanassiou, "A tutorial on synthetic aperture radar," *IEEE Geosci. Remote Sens. Mag.*, vol. 1, no. 1, pp. 6–43, Mar. 2013, doi: 10.1109/MGRS.2013.2248301.
[14] H. Rott, "The analysis of backscattering properties from SAR data of mountain regions," *IEEE J. Ocean. Eng.*, vol. 9, no. 5, pp. 347–355, Dec. 1984, doi: 10.1109/JOE.1984.1145655.
[15] C. Màtzler, "Microwave sensors for measuring avalanche-critical snow parameters," *IAHS Pub.*, no. 162, pp. 149–160, 1987.
[16] J. Zhu, S. Tan, J. King, C. Derksen, J. Lemmetyinen, and L. Tsang, "Forward and inverse radar modeling of terrestrial snow using SnowSAR data," *IEEE Trans. Geosci. Remote Sens.*, vol. 56, no. 12, pp. 7122–7132, Dec. 2018, doi: 10.1109/TGRS.2018.2848642.
[17] L. D. Gregorio et al., "SWE retrieval by exploiting COSMO-SkyMed X-band SAR imagery and ground data through a machine learning approach," in *Proc. Act. Passive Microw. Remote Sens. Environ. Monit. III*, 2019, vol. 11154, pp. 38–48, doi: 10.1117/12.2550824.
[18] H. Rott et al., "Development of snow retrieval algorithms for CoReH2O—grain size estimator," Executive Summary, 2013.
[19] S. Leinss, O. Antropov, J. Vehvilaeinen, J. Lemmetyinen, I. Hajnsek, and J. Praks, "Wet snow depth from TanDEM-X single-pass inSAR DEM differencing," in *Proc. IEEE Int. Geosci. Remote Sens. Symp.*, 2018, pp. 8500–8503, doi: 10.1109/IGARSS.2018.8518661.
[20] J. Shi and J. Dozier, "Estimation of snow water equivalence using SIR-C/X-SAR. I. Inferring snow density and subsurface properties," *IEEE Trans. Geosci. Remote Sens.*, vol. 38, no. 6, pp. 2465–2474, Nov. 2000, doi: 10.1109/36.885195.

[21] H. Lievens et al., "Snow depth variability in the Northern Hemisphere mountains observed from space," *Nature Commun.*, vol. 10, pp. 1–12, 2019, doi: 10.1038/s41467-019-12566-y.

[22] T. Guneriussen, K. A. Hogda, H. Johnsen, and I. Lauknes, "InSAR for estimation of changes in snow water equivalent of dry snow," *IEEE Trans. Geosci. Remote Sens.*, vol. 39, no. 10, pp. 2101–2108, Oct. 2001, doi: 10.1109/36.957273.

[23] S. Leinss, A. Wiesmann, J. Lemmetyinen, and I. Hajnsek, "Snow water equivalent of dry snow measured by differential interferometry," *IEEE J. Sel. Topics Appl. Earth Observ. Remote Sens.*, vol. 8, no. 8, pp. 3773–3790, Aug. 2015, doi: 10.1109/JSTARS.2015.2432031.

[24] J. J. Ruiz et al., "Investigation of environmental effects on coherence loss in SAR interferometry for snow water equivalent retrieval," *IEEE Trans. Geosci. Remote Sens.*, vol. 60, 2022, Art. no. 4306715, doi: 10.1109/TGRS.2022.3223760.

[25] H. Li, Z. Wang, G. He, and W. Man, "Estimating snow depth and snow water equivalence using repeat-pass interferometric SAR in the northern piedmont region of the Tianshan mountains," *J. Sensors*, vol. 2017, 2017, doi: 10.1155/2017/8739598.

[26] V. Conde, C. Nico, P. Mateus, J. Catalao, A. Kontu, and M. Gritsevich, "On the estimation of temporal changes of snow water equivalent by spaceborne SAR interferometry: A new application for the Sentinel-1 mission," *J. Hydrol. Hydromechanics*, vol. 67, no. 1, pp. 93–100, 2019, doi: 10.2478/johh-2018-0003.

[27] P. N. Dagurov, T. N. Chimitdorzhiev, A. V. Dmitriev, and S. I. Dobrynin, "Estimation of snow water equivalent from L-band radar interferometry: Simulation and experiment," *Int. J. Remote Sens.*, vol. 41, no. 24, pp. 9328–9359, Dec. 2020, doi: 10.1080/01431161.2020.1798551.

[28] A. T. Torun and S. EkerciN, "Estimating snow density, depth, volume, and snow water equivalent with InSAR data in the Erciyes mountain/Turkey," *Arabian J. Geosci.*, vol. 14, no. 15, Aug. 2021, Art. no. 1456, doi: 10.1007/s12517-021-07873-y.

[29] A. Wiesmann and C. Mätzler, "Microwave emission model of layered snowpacks," *Remote Sens. Environ.*, vol. 70, no. 3, pp. 307–316, 1999, doi: https://doi.org/10.1016/S0034-4257(99)00046-2.

[30] R. Bamler and P. Hartl, "Synthetic aperture radar interferometry," *Inverse Problems*, vol. 14, no. 4, pp. R1–R54, Aug. 1998, doi: 10.1088/0266-5611/14/4/001.

[31] Finnish Meteorological Institute, "Data from the artic space centre." Accessed: Oct. 30, 2020. [Online]. Available: https://litdb.fmi.fi/ioa_snow-water-equivalent.php

[32] Finnish Meteorological Institute, "Data from the artic space centre." Accessed: Oct. 30, 2020. [Online]. Available: https://litdb.fmi.fi/ioa0003_data.php

[33] P. Prats et al., "Taxi: A versatile processing chain for experimental TanDEM-X product evaluation," in *Proc. IEEE Int. Geosci. Remote Sens. Symp.*, 2010, pp. 4059–4062, doi: 10.1109/IGARSS.2010.5651002.

[34] A. Ferretti, C. Prati, and F. Rocca, "Permanent scatterers in SAR interferometry," *IEEE Trans. Geosci. Remote Sens.*, vol. 39, no. 1, pp. 8–20, Jan. 2001, doi: 10.1109/36.898661.

[35] P. Berardino, G. Fornaro, R. Lanari, and E. Sansosti, "A new algorithm for surface deformation monitoring based on small baseline differential SAR interferograms," *IEEE Trans. Geosci. Remote Sens.*, vol. 40, no. 11, pp. 2375–2383, Nov. 2002, doi: 10.1109/TGRS.2002.803792.

[36] S. Leinss, G. Parrella, and I. Hajnsek, "Snow height determination by polarimetric phase differences in X-band SAR data," *IEEE J. Sel. Topics Appl. Earth Observ. Remote Sens.*, vol. 7, no. 9, pp. 3794–3810, Sep. 2014, doi: 10.1109/JSTARS.2014.2323199.

[37] H. Rott, T. Nagler, and R. Scheiber, "Snow mass retrieval by means of SAR interferometry," in *Proc. FRINGE Workshop*, 2003, pp. 1–6.

[38] M. Schwank, M. Stahli, H. Wydler, J. Leuenberger, C. Matzler, and H. Fluhler, "Microwave L-band emission of freezing soil," *IEEE Trans. Geosci. Remote Sens.*, vol. 42, no. 6, pp. 1252–1261, Jun. 2004, doi: 10.1109/TGRS.2004.825592.

[39] Corine Land Cover, "Copernicus land monitoring service," 2018. Accessed: May 22, 2023. [Online]. Available: https://doi.org/10.2909/960998c1-1870-4e82-8051-6485205ebbac

[40] K. Kellogg et al., "NASA-ISRO synthetic aperture radar (NISAR) mission," in *Proc. IEEE Aerosp. Conf.*, 2020, pp. 1–21, doi: 10.1109/AERO47225.2020.9172638.

[41] M. W. J. Davidson and R. Furnell, "ROSE-L: Copernicus L-band SAR mission," in *Proc. IEEE Int. Geosci. Remote Sens. Symp.*, 2021, pp. 872–873, doi: 10.1109/IGARSS47720.2021.9554018.

Kristina Belinska (Graduate Student Member, IEEE) received the B.Sc. and M.Sc. degrees in physics from the University of Bremen, Bremen, Germany, in 2017 and 2019, respectively. Since 2020, she has been working toward the Ph.D. degree in environmental engineering with the Swiss Federal Institute of Technology (ETH Zurich), Zurich, Switzerland.

In 2019, she joined the Polarimetric SAR Interferometry (Pol-InSAR) group, Microwaves and Radar Institute, German Aerospace Space Center (DLR), Wessling, Germany. Her main research interests include the retrieval of snow parameters from repeat-pass interferometric, multifrequency, and polarimetric synthetic aperture radar data.

Georg Fischer received the B.Sc. and M.Sc. degrees in geography from the Ludwig Maximilians University of Munich, Munich, Germany, in 2009 and 2012, respectively, and the Ph.D. degree in environmental engineering from the Swiss Federal Institute of Technology (ETH Zurich), Zurich, Switzerland in 2019.

From 2012 to 2013, he conducted a traineeship with the Mission Science Division, Directorate of Earth Observation Programmes, European Space Agency, Noordwijk, The Netherlands. In 2013, he joined the Polarimetric Synthetic Aperture Radar Interferometry Research Group, Radar Concepts Department, Microwaves and Radar Institute, German Aerospace Center (DLR), Wessling, Germany. His research interests include the characterization and modeling of interferometric and tomographic synthetic aperture radar (SAR) measurements from snow and ice and the development of methods for the estimation of geophysical properties of glaciers and ice sheets from polarimetric and interferometric SAR data.

Giuseppe Parrella received the B.Sc. and M.Sc. degrees in telecommunications engineering from the University of Naples Federico II, Naples, Italy, in 2007 and 2010, respectively, and the Ph.D. degree in environmental engineering from the Swiss Federal Institute of Technology (ETH Zurich), Zurich, Switzerland, in 2015.

From 2010 to 2021, he was the Polarimetric Interferometry Synthetic Aperture Radar (PolInSAR) Research Group, German Aerospace Center (DLR), Wessling, Germany. Between 2021 and 2023, he was with the Marketing and Sales Department, Thales Alenia Space, Rome, Italy. His focus was on the development of industrial strategy and capture of business opportunities in the context of ESA radar satellite missions. Since January 2023, he has been with the Mission Management and Ground Segment Department, Earth Observation Programmes (EOP) Directorate, European Space Agency (ESA), ESA-ESRIN, Frascati, Italy. His research interests include electromagnetic modeling of ice and snow scattering properties, radar polarimetry, and polarimetric interferometry.

Irena Hajnsek (Fellow, IEEE) received the Dipl. (Hons.) degree in fluvial river systems from the Free University of Berlin, Berlin, Germany, in 1996, and the Dr. rer. nat. (Hons.) degree in model-based estimation of soil moisture from fully polarimetric synthetic aperture radar from the Friedrich Schiller University of Jena, Jena, Germany, in 2001.

Since 2009, she has been a Professor of earth observation with Zürich Institute of Environmental Engineering, Swiss Federal Institute of Technology (ETH), Zürich, Switzerland, and at the same time, the Head of the Polarimetric SAR Interferometry Research Group, German Aerospace Center Microwaves and Radar Institute, Wessling, Germany. Her main research interests include electromagnetic propagation and scattering theory, radar polarimetry, SAR and interferometric SAR data processing techniques, environmental parameter modeling and estimation.

Prof. Hajnsek has been the Science Coordinator of the German satellite mission TanDEM-X, since 2010. She is currently a Member of the European Space Agency Mission Advisory Group, ROSE-L Mission. She was the Technical Program Cochair of the IEEE International Symposium on Geoscience and Remote Sensing (IGARSS) in 2012, in Munich, Germany, and in 2019, in Yokohama, Japan. From 2013 to 2021, she was a Member of the IEEE GRSS AdCom, and from 2016 to 2020, the Vice President of the IEEE GRSS Technical Committees. She is the founder of the new Technical Committee Remote sensing Environment, Analysis and Climate Technologies (REACT) in 2021.